Enhanced Efficiency of Hot-Cast Large-Area Planar Perovskite Solar Cells/Modules Having Controlled Chloride Incorporation

Hsueh-Chung Liao, Peijun Guo, Che-Pu Hsu, Ma Lin, Binghao Wang, Li Zeng, Wei Huang, Chan Myae Myae Soe, Wei-Fang Su, Michael J. Bedzyk, Michael R. Wasielewski, Antonio Facchetti, Robert P. H. Chang, Mercouri G. Kanatzidis,* and Tobin J. Marks**

Organic–inorganic perovskite photovoltaics are an emerging solar technology. Developing materials and processing techniques that can be implemented in large-scale manufacturing is extremely important for realizing the potential of commercialization. Here we report a hot-casting process with controlled Cl^- incorporation which enables high stability and high power-conversion-efficiencies (PCEs) of 18.2% for small area (0.09 cm^2) and 15.4% for large-area (≈1 cm^2) single solar cells. The enhanced performance versus tri-iodide perovskites can be ascribed to longer carrier diffusion lengths, improved uniformity of the perovskite film morphology, favorable perovskite crystallite orientation, a halide concentration gradient in the perovskite film, and reduced recombination by introducing Cl^-. Additionally, Cl^- improves the device stability by passivating the reaction between I^- and the silver electrode. High-quality thin films deployed over a large-area 5 cm × 5 cm eight-cell module have been fabricated and exhibit an active-area PCE of 12.0%. The feasibility of material and processing strategies in industrial large-scale coating techniques is then shown by demonstrating a "dip-coating" process which shows promise for large throughput production of perovskite solar modules.

1. Introduction

Perovskite solar cells have attracted great interest because of their adaptability to solution processing, tunability of optoelectronic properties, achievement of high power-conversion-efficiencies (PCEs), etc.[1–4] The ambipolar semiconducting methylammonium lead tri-iodide ($MAPbI_3$) has dominated perovskite research activity over the past few years and can be employed in various device architectures, for example, p-i-n planar structures, oxide-based mesoporous structures, etc.[1–4] The p-i-n planar structure, specifically the inverted type in which the p-type coated transparent conducting oxide (TCO) lies below the perovskite absorber, has recently shown great promise because of its simplified fabrication and reduced hysteresis effects in current–voltage response.[5] Although the record

Dr. H.-C. Liao, M. Lin, B. Wang, W. Huang, C. M. M. Soe, Prof. M. R. Wasielewski, Dr. A. Facchetti, Prof. M. G. Kanatzidis, Prof. T. J. Marks
Department of Chemistry
Northwestern University
Evanston, IL 60208, USA
E-mail: m-kanatzidis@northwestern.edu; t-marks@northwestern.edu

Dr. H.-C. Liao, C.-P. Hsu
FrontMaterials Corporation Ltd.
Taipei 10087, Taiwan

Dr. H.-C. Liao, Dr. P. Guo, Dr. M. Lin, C. M. M. Soe, Prof. M. R. Wasielewski, Prof. R. P. H. Chang, Prof. M. G. Kanatzidis, Prof. T. J. Marks
Argonne-Northwestern Solar Energy Research Center
Northwestern University
Evanston, IL 60208, USA
E-mail: r-chang@northwestern.edu

Dr. P. Guo, Prof. M. J. Bedzyk, Prof. R. P. H. Chang
Department of Materials Science and Engineering
Northwestern University
Evanston, IL 60208, USA

C.-P. Hsu, Prof. W.-F. Su
Department of Materials Science and Engineering
National Taiwan University
Taipei 10617, Taiwan

L. Zeng, Prof. M. J. Bedzyk
Applied Physics Program and the Materials Research Center
Northwestern University
Evanston, IL 60208, USA

Dr. A. Facchetti
Polyera Corporation
Skokie, IL 60077, USA

DOI: 10.1002/aenm.201601660

efficiencies >22% have been reached in the NREL solar cell efficiency chart, device areas are still small, <0.1 cm^2, raising issues such as measurement contacts, film uniformity, peripheral effects, etc.[3,5–7] The availability of large-area cells/modules and their performance characterization are thus critical to evaluating newly developed processing techniques and materials for future commercialization. For successful implementation of large-area cells, the p-i-n planar device architecture is of great promise for its low temperature/fewer steps processing and realization of efficiencies >19%.[8,9] Chen et al. recently certified a p-i-n planar perovskite solar cell of 15.0% PCE with a cell area >1 cm^2 which was the first perovskite photovoltaic record listed in the Solar Cell Efficiency Tables.[5,6] Of various film fabrication methods introduced to the field, the solvent-engineering process has been heavily used[5,10] in which the perovskite precursor solution is spin-coated onto the substrate followed by dropping anti-solvent during the substrate spinning. Nevertheless, we find that spinning off of the anti-solvent greatly limits the spin-coating technique since it is difficult to perform the solvent washing steps with industrial scale coating techniques such as slot-die coating, spray coating, doctor blade coating, dip-coating, etc. In contrast, techniques based on temperature control are more practical and mature for manufacturing scale equipment.

Hot-casting, in which the perovskite solution is coated on a pre-heated substrate, represents a promising processing strategy in commercial coating techniques for large throughput, ultrafast production.[11–14] Conventionally, pre-heated substrates are used to facilitate the film formation and crystallization while still requiring post thermal treatments. Recently, Nie et al. reported the first example where high-quality, large-sized perovskite grains grow rapidly on a preheated substrate without post-treatment, namely, a one-step process which promises rapid, high throughput production, using methylammoniun chloride (MACl) and lead iodide (PbI_2).[12] In subsequent work, these authors also incorporated I_2 or methylammonium iodide (MAI) in the precursor solution as an additive to the MACl + PbI_2 precursor to suppress the undesired methylammonium lead trichloride ($MAPbCl_3$) formation. $MAPbCl_3$ has a large bandgap (>2.97 eV)[15] and fails to contribute to photocurrent beyond the ultraviolet region of the solar spectrum, and can cause significant irregularities in device performance.[11] However, in both cases using MACl as the major precursor yield various amounts of $MAPbCl_3$ in addition to the photoactive $MAPbI_3$ phase. The $MAPbCl_3$ phase is also produced in other processing methods utilizing Cl^- precursors.[16–19] In contrast, it is known that the Cl^--derived perovskite compound ($MAPbI_{3-x}Cl_x$) having small amounts of residual Cl^- (x < 0.05 at%) possesses superior optoelectronic properties.[20–27] Specifically, trace controlled Cl^- incorporation into the perovskite crystals improves the morphology,[21–23,28] increases the carrier diffusion length,[24–26] passivates trap states,[29] and enhances crystallinity[25] as compared to pure $MAPbI_3$. However, control of the Cl^- content is challenging in the aforementioned processing approaches, owing to the poorly defined sublimation characteristics of Cl^- sources such as MACl or ambiguous crystallization kinetics.[20,22,30,31] Consequently, developing a reliable process for controlling Cl^- incorporation while preventing deleterious $MAPbCl_3$ formation is important for achieving high PCEs and highly reproducible devices/modules for further scale-up. Hot-casting is therefore promising for such compositional engineering due to the ultrafast crystallization rate for preserving the incorporated elements.

Here we report a one-step hot-casting perovskite system with controlled Cl^- incorporation to achieve a high PCE of 18.2%. The PbI_2 + MAI were chosen as the major precursors, and various amounts of the Cl^- precursors $PbCl_2$ + MACl in stoichiometric ratio (3, 5, 10, and 20 at%) with respective to the major precursors are included as additives for better controlling the Cl^- incorporation (cf., Experimental Section and Table S1, Supporting Information). Compared to the aforementioned tri-iodide perovskite with PCE = 15.5%, the enhancement with 3–5 at% Cl^- incorporation can be attributed to longer carrier diffusion lengths, improved perovskite film morphology, preferred orientation of perovskite crystallites, a halide concentration gradient throughout the perovskite film, and reduced recombination. Additionally, Cl^- plays a role in increasing device stability by passivating the reaction between I^- and the silver electrode. Furthermore, we report scaling up the single cell area to ≈1 cm^2 with PCE of 15.4%. A 5 cm × 5 cm eight-cell module is also fabricated with an active-area PCE of 12.0%. Finally, a "hot dip-coating" process is representatively chosen, among the large-scale coating techniques, for demonstrating the viability of the present hot-casting system in high throughput coating techniques, highlighting its promise for perovskite solar module production (Supporting Information).

2. Results and Discussion

Perovskite film processing begins with the $MAPbI_3$ tri-iodide compound hot-cast from stoichiometric PbI_2 and MAI salts (1:1 molar ratio) instead of the conventional PbI_2 and MACl.[11,12] Various amounts (3–20 at% with respect to PbI_2 + MAI) of the $PbCl_2$ and MACl chloride precursors are additionally introduced into the PbI_2 + MAI pure-iodide precursor solutions. The details of the solution preparation can be found in the Experimental Section and Table S1 (Supporting Information). This precursor system enables a better control of the Cl^- incorporation compared to the conventional PbI_2 and MACl, which leads to excess undesirable $MAPbCl_3$ phase formation. The increase in light harvesting can be clearly seen by the film color in the photographic images (Figure S1, Supporting Information) where the PbI_2 + MAI perovskite film is dark brown while the PbI_2 + MACl film is lighter and semi-transparent at similar film thicknesses (≈350 nm). Note that the composition percentages are the incorporation ratio of the precursors and nominal for the final perovskite products.

Chloride precursors remarkably affect the crystallization kinetics during film deposition in conventional perovskite processing approaches.[23] Here we investigate the impact of undesirable $MAPbCl_3$ phase formation on the morphology of hot-cast perovskite films. Optical microscopy (OM), scanning electron microscopy (SEM), and atomic force microscopy (AFM) images of $MAPbI_3$ with varying amounts of added Cl^- are presented in **Figure 1** top, middle, and bottom rows, respectively. The OM images of the Cl^--free $MAPbI_3$ film reveal poor surface coverage with large densities of pinholes (bright regions).

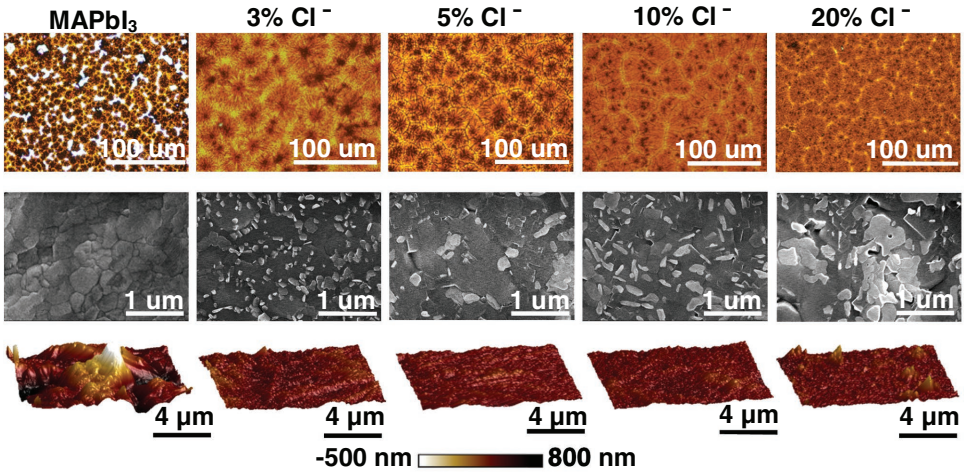

Figure 1. Morphological characterization of perovskite $MAPbI_3$ films without and with 3%, 5%, 10%, and 20 at% Cl^- incorporation by optical microscopy (top row), SEM (middle row), and AFM (bottom row).

In contrast, Cl^- incorporation at >3 at% significantly enhances film uniformity, with continuous coverage across the entire surface. More closely examining the microstructure by SEM reveals that all of the perovskite films have tightly packed grains with grain sizes ranging from hundreds of nm to 1 μm. Note that a precipitate forms as seen in the SEM images (Figure 1, middle row), spreading over the Cl^--containing perovskite grains, and their density as well as dimensions increase with increased Cl^- loading. The faceted precipitates in the heavily Cl^--incorporated perovskite films (20 at%) create tattered and non-uniform surfaces. The line scans from SEM energy dispersive spectroscopy (EDS; Figure S2, Supporting Information) on a 10 at% Cl^- incorporated perovskite film indicate that these precipitates are chlorine-rich.

To complement the bulk sensitive SEM-EDS measurements, surface-sensitive X-ray photoelectron spectroscopy (XPS) was also performed (Figure S3, Supporting Information) using ion sputtering. A clear distribution gradient of the halide elements throughout the perovskite films is observed where the top surface is Cl^--rich while the material closer to the substrate is I^--rich. Surprisingly, such a Cl^-/I^- distribution is opposite to that of conventional n-i-p device cell architectures in which Cl^- preferentially distributes closer to the TiO_2 substrates.[32–34] We speculate that the crystallization kinetics and substrate halide affinity play important roles in the present case. The included Cl^- precursors tend to naturally aggregate due to lower solubility.[16,28] Unlike conventional processing methods in which the Cl^--derived compounds appear to serve as a template,[23] in the hot-casting approach the solvent dries instantly upon contact with the hot substrates and draws the pre-aggregated Cl^--rich domains toward the surfaces. Consequently, the rapid crystallization creates a gradient of halide distribution as well as morphological changes, with small grains distributing over the surfaces. From an electronic perspective, the Cl^- at the perovskite–electron transporting layer interfaces ($PC_{61}BM$ is on top) is advantageous for directional electron extraction due to the conduction band bending.[32]

AFM images further assist to clarify the film surface topography. With controlled Cl^- incorporation ranging from 3 to ≈10 at%, the perovskite films are significantly smoothed versus the Cl^--free films, with remarkably reduced root-mean-square (rms) roughnesses, i.e., from 216 nm for $MAPbI_3$ to 49.9, 32.2, and 36.8 nm for 3, 5, and 10 at% Cl^- incorporation, respectively. Over-loading Cl^- (20 at%) however erodes the surface uniformity with large fragments of perovskite appearing on top and an rms roughness of 51.9 nm, consistent with the SEM image.

Figure 2a shows X-ray diffraction (XRD) patterns of the tri-iodide perovskite films and perovskite films with varying amounts of Cl^- incorporation. The simulated patterns for $MAPbI_3$ and $MAPbCl_3$, and the pattern for the fluorine-doped tin oxide (FTO) substrate are presented for comparison. Accordingly, the tri-iodide perovskite exhibits a tetragonal I4 cm crystal structure in which the Bragg peaks at 14.14°, 20.05°, 23.54°, 28.51°, and 31.96° can be assigned to the (110), (020), (121), (220), and (130) planes of the $MAPbI_3$ crystallites, respectively.[35] Increasing the amount of Cl^- leads to remarkably enhanced (110) scattering intensity while the (020) intensity is reduced, indicating that Cl^- incorporation promotes a preferred perovskite (110) orientation with the *c*-axis perpendicular to the substrate. Such (110) oriented structures have also been observed in other processing methods for high-efficiency Cl^--derived perovskite solar cells.[28,36,37] Additionally, the (110) Bragg peak shown in expanded scale in Figure 2b shows slight shifts with Cl^- incorporation, suggesting subtle contraction of the *c*-axis, and providing evidence that the Cl^- is doped into the perovskite crystal structure (i.e., $MAPbI_{3-x}Cl_x$) at apical sites in the Pb coordination octahedron.[37,38] For the Cl^- doping in the $MAPbI_3$ materials x is <0.04,[17] and the Cl^- incorporation induces the formation of two secondary phases, PbI_2 and $MAPbCl_3$, as indicated by the appearance of Bragg peaks at 12.70° and 15.60°, respectively. Note that PbI_2 can potentially enhance the photovoltaic properties by suppressing carrier recombination at grain boundaries.[39,40] In contrast, the $MAPbCl_3$ is ineffective in light harvesting due to its large bandgap, especially at high Cl^- loadings of ≈20 at%. In principle, when Cl^- precursors are used in the perovskite solution, Cl^- can either: (1) chemically *dope* into the $MAPbI_3$ to form $MAPbI_{3-x}Cl_x$ or (2) form the $MAPbCl_3$

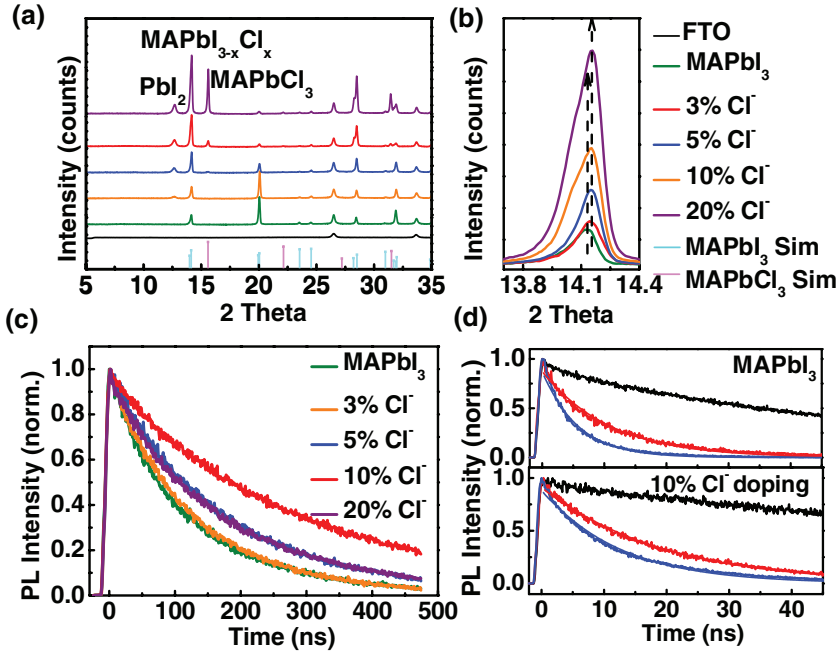

Figure 2. Characterization of perovskite $MAPbI_3$ films without and with 3%, 5%, 10%, and 20 at% Cl^- incorporation. a) XRD diffraction patterns. b) Expansion of XRD pattern, focusing on the $MAPbI_{3-x}Cl_x$ perovskite (110) Bragg reflection. c) TRPL curves for pristine perovskite films. d) Representative modeling of carrier lifetimes by TRPL of the indicated pristine perovskite films (black) and, respectively, in conjunction with a hole quencher (red) and an electron quencher (blue).

phase. For Cl^- concentrations <10 at%, the doping mechanism (mode (1)) dominates. The two modes of Cl^- incorporation are not uniformly distributed across the film according to depth profiling, and Cl^--rich regions are close to the surface (Figure S3, Supporting Information).

The predominant form of electrons and holes in $MAPbI_3$ are expected to be free carriers because the excitons are weakly bound and easily dissociated at room temperature.[41] Hence, the decay of the radiative species measured here by time-resolved photoluminescence (TRPL) represents the decay of free carriers in the perovskite film. The TRPL of the present perovskite films as a function of Cl^- concentration is plotted in Figure 2c. Exponential fitting gives decay times of 85.5, 105.5, 148.1, 242.1, and 138.1 ns for $MAPbI_3$, with 3, 5, 10, and 20 at% Cl^- incorporation, respectively. Apparently, using <10 at% Cl^- enhances the carrier lifetime by 2–3× versus $MAPbI_3$, consistent with the literature for films fabricated by the conventional process.[24] Note that the carrier lifetime depends not only on composition but also on morphology where defects, grain boundaries, surface states, etc., induce recombination.[42] The drop in carrier lifetime in the heavily Cl^--loaded perovskite films (≈20 at%) likely results from significant phase impurities (e.g., $MAPbCl_3$) and the rough morphologies (Figure 1).

The carrier diffusion lengths of perovskite films can be determined by employing the diffusion model for a bi-layer structure,[24,25] that is, perovskite/carrier quencher. The TRPL of $MAPbI_3$ and a perovskite film with 10% Cl^- in a bilayer having the hole quencher (poly(3,4-ethylenedioxythiophene) polystyrene sulfonate, PEDOT:PSS) and electron quencher (phenyl-C61-butyric acid methyl ester, PCBM) respectively, are shown in Figure 2d. Accordingly, the estimated carrier diffusion lengths increase from 507 to 661 nm for holes and from 720 to 825 nm for electrons. The increase in both carrier lifetime and carrier diffusion length achieved in the present work should be advantageous in reducing recombination from charge extraction (CE) by electron/hole conducting layers, and thus enhancing device performance.

An inverted p-i-n planar architecture was employed for the solar cells as shown in **Figure 3**a. Solution-processed p-type nickel oxide (NiO_x)[43] served as the substrate, followed by various perovskite compositions, that is, $MAPbI_3$, 3 at% Cl^-, 5 at% Cl^-, 10 at% Cl^-, and 20 at% Cl^- incorporation, respectively, an n-type electron transporting layer, PCBM, and a polyethylenimine (PEI)/Ag electrode (see the Experimental Section for details). Figure 3b presents a cross-sectional transmission electron microscopy (TEM) image of a solar cell (10 at% Cl^-) with the sample prepared by focused ion beam techniques. Note that the perovskite grains are continuous throughout the film with a thickness of ≈400 nm and in junctions having ≈60–70 nm layers of PCBM and NiO_x. Figure 3c shows the effects of Cl^- precursors in the hot-cast perovskite films on the current density–voltage response curves of perovskite solar cells. These curves were measured in a reverse scan direction from V_{oc} to the J_{sc} under simulated AM1.5 sunlight. The corresponding photovoltaic characteristics of V_{oc}, J_{sc}, and fill factor (FF), averaged PCEs, and champion PCEs are summarized in **Table 1**. Statistical analysis was carried out for ten devices fabricated from at least three independent fabrication runs.

Remarkably, incorporating Cl^- at 5–10 at% nominal fractions enhances the overall PCEs from 15.5% to 17–18% (champion device = 18.2%). The increase in device performance is mainly attributed to the increased V_{oc} and FF. Over-incorporating Cl^- up to 20 at% dramatically reduces the PCEs because of decreased J_{sc}. Figure 3d plots the corresponding external quantum efficiency (EQE) spectra which consistently show good agreement between integrated J_{sc}'s and the values obtained from J–V scans. Accordingly, the $MAPbI_3$ and 3–10 at% Cl^- incorporated perovskite devices display broad EQE plateaus through the visible to near-infrared range. Note also that the Cl^- inclusion, even at low levels of 3 at%, leads to a blue shift of the EQE spectrum. This indicates that the perovskite bandgap is slightly enlarged upon Cl^- incorporation,[44] supporting the XRD results that some Cl^- ions are chemically doped (mode (1)) to form the $MAPbI_{3-x}Cl_x$ perovskite structure. The blue shift suggests that the bandgap $MAPbI_{3-x}Cl_x$ is enlarged compared to $MAPbI_3$, consistent with the results of Chae et al.[44] Additionally, the larger bandgap and increased conductance also contribute to the enhanced V_{oc} from 1022 mV for the $MAPbI_3$ device to 1113 mV for the 20 at% Cl^- incorporated devices. In summary, the substantially enhanced V_{oc}, FF, and thus PCE values in the perovskite 5–10 at% Cl^- incorporation range reflect a

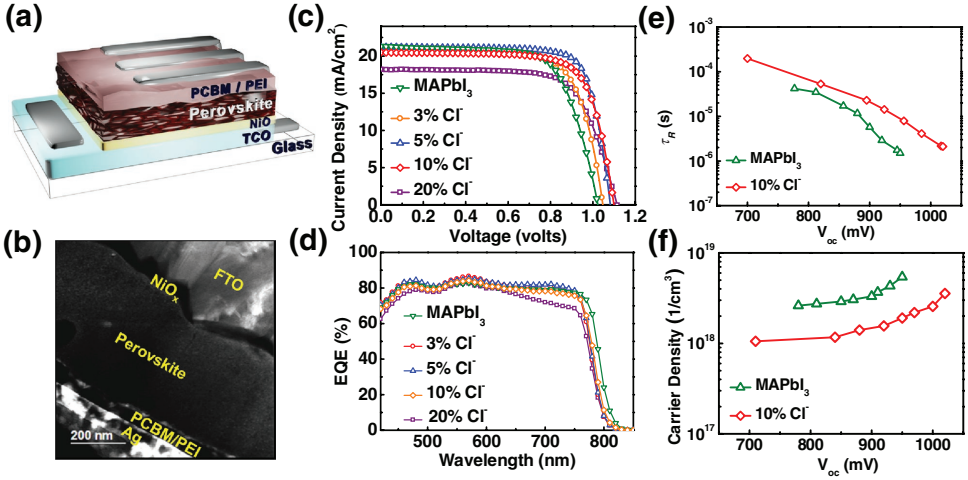

Figure 3. Planar structure perovskite solar cells and their photovoltaic and kinetic response. a) Illustration of inverted planar device architecture, TCO/NiO/perovskite/$PC_{61}BM$/PEI/Ag. b) Cross-sectional TEM image of a solar cell using a perovskite with 10 at% Cl^- incorporations. c) *J–V* curves. d) EQE characteristics of the perovskite solar cells with the indicated Cl^- incorporations. e) Recombination time constant τ_R and f) carrier density *n* of a $MAPbI_3$ perovskite film without and with 10 at% Cl^- incorporation, and the dependence on V_{oc}.

combination of effects arising from: (1) passivation of surface recombination by PbI_2, (2) band bending from the gradient in Cl^- film distribution which facilitates electron injection, (3) enhanced carrier lifetimes and carrier diffusion lengths, (4) preferred (110) orientation with better carrier conductance, and (5) uniform perovskite film morphology. It is noteworthy that excess chloride (20 at%) leads to dramatically decreased PCE and a dip in the EQE response at wavelengths >600 nm. We speculate the reduced efficiency can be ascribed to the non-uniform surface, the presence of the $MAPbCl_3$ phase impurity, etc. Perovskite solar cells are notorious for hysteresis when measurements are performed in different scanning directions. The present high-PCE devices were examined in both scanning directions (Figure S4, Supporting Information) and exhibit negligible hysteresis as a result of passivation by $PC_{61}BM$.[45]

To gain further insight into the performance enhancement by Cl^- incorporation, we characterized the kinetics of device response by transient photovoltage (TPV) and CE measurements in $MAPbI_3$ devices with and without 10% Cl^- incorporation. Recombination time constants, τ_R and carrier densities, *n* were extracted from the TPV and CE data, respectively (Figure 3e,f). The device with Cl^- incorporation shows substantially longer τ_R, confirming the reduced carrier recombination in the perovskite, in good correlation with the enhanced device performance (Table 1) versus $MAPbI_3$. The slightly lower carrier density of the Cl^--containing perovskite film suggests that even small amounts of the wide bandgap $MAPbCl_3$ phase (Figure 2a) decrease the number of photogenerated carriers under illumination. This is consistent with the *J–V* results showing that the 10% Cl^- device exhibits slightly reduced current density (≈20.5 mA cm^{-2}) versus that of $MAPbI_3$ (≈21.3 mA cm^{-2}). The optimized Cl^- amount of 3%–5% is thereby critical for achieving high performance.

Table 1. Photovoltaic performance of $MAPbI_3$ perovskite solar cells without and with various levels of Cl^- incorporation. Statistical analysis was carried out for ten devices fabricated from at least three independent preparation runs.

Perovskite	J_{sc} [mA cm^{-2}]	V_{oc} [mV]	FF [%]	PCE [%]
$MAPbI_3$	21.3	1022	71.2	15.5 (14.7 ± 0.70)
3% Cl^-	21.2	1058	75.5	16.9 (15.8 ± 0.95)
5% Cl^-	21.2	1085	79.2	18.2 (17.8 ± 0.52)
10% Cl^-	20.5	1101	78.1	17.8 (17.3 ± 0.55)
20% Cl^-	18.2	1113	73.5	14.9 (13.2 ± 1.61)

Based on the above results and considerations, solar cells with areas larger than 1 cm^2 were fabricated using a perovskite precursor solution with 5 at% Cl^- incorporation. The *J–V* response of the solar cell is plotted in **Figure 4**a, with a device image shown in the inset. We used a square device layout of 1 cm × 1 cm and obtained excellent photovoltaic parameters of J_{sc} = 21.0 mA cm^{-2}, V_{oc} = 1.06 V, FF = 69.1%, and PCE = 15.4%. The corresponding EQE spectrum (Figure 4b) again shows a broad plateau and is consistent with the integrated current density from the *J–V* measurements. The device shows negligible hysteresis effects as shown in Figure S4b (Supporting Information). The reduced efficiency from 18.2% for 0.09 cm^2 to 15.4% for 1 cm^2 cells can be attributed to the reduced electrode conductivity[46] and the greater possibility of defect formation in large-area thin films. Further improvements can be expected by using a metallic-doped NiO substrate or rectangular cell layout to reduce the resistance loss from the FTO substrate. We also fabricated a module having eight cells connected in series (cf., Experimental Section for fabrication details and device layout shown in Figure S5, Supporting Information). Thus, a blade-scribed module was created on a 5 cm × 5 cm substrate with a geometric fill factor ≈60%, shown in Figure 4c inset. This module exhibits high active-area PCE parameters of J_{sc} = 2.60 mA cm^{-2}, V_{oc} = 7.98 V, FF = 58.2%, and PCE = 12.0%.

Preliminary cell stability tests were next performed for the present devices using 85 °C/65 RH% thermal damping conditions, without sealing the cell. The images of the cells

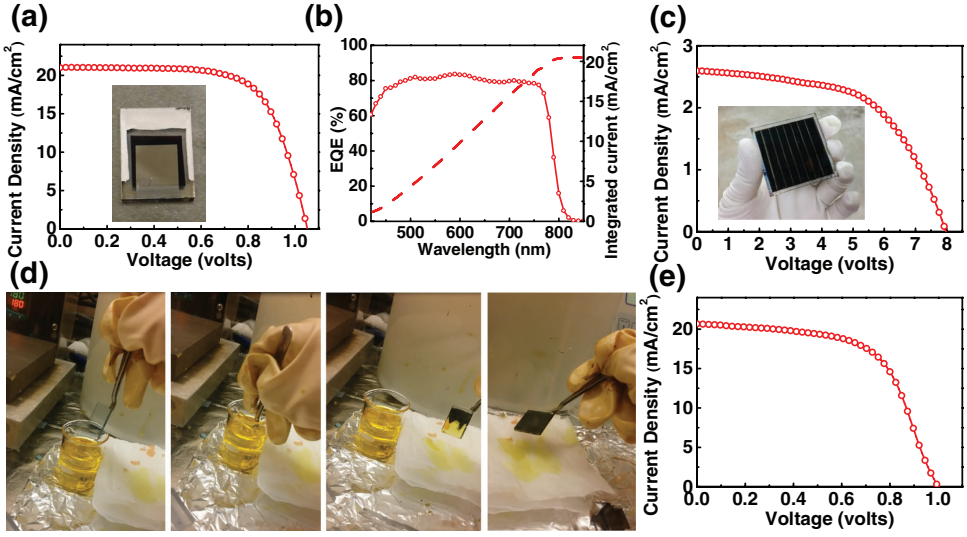

Figure 4. Perovskite film solar cells/modules based on films with optimized Cl^- incorporation ≈5 at%. a) *J–V* response curve of ≈1 cm^2 solar cell with its image shown in the inset. b) EQE spectrum of ≈1 cm^2 solar cell and current density integration based on the A.M. 1.5 spectrum. c) *J–V* curve of a 5 cm × 5 cm, eight-cell connected module with its image shown in the inset. d) Pictures of the hot dip-coating process. The entire process is shown in the attached video in the Supporting Information. e) *J–V* curve of the perovskite solar cell prepared by hot dip-coating.

after aging for 40 h (Figure S6, Supporting Information) clearly show that the silver electrode on $MAPbI_3$ turns black, whereas the silver electrode remains shiny on the Cl^- incorporated perovskite devices. Thus, the $MAPbI_3$ cell was significantly degraded while the 10% Cl^- incorporated devices retained >70% of PCE after 40 h aging (Figure S6, Supporting Information). These results indicate that Cl^- incorporation, which preferentially distributes on the perovskite surfaces, stabilizes the device. It has been reported that the perovskite solar cells are dramatically degraded by the reaction of the metal electrode with I^- from the perovskite,[47] particularly in humid environments. We speculate that the degradation may reflect a combination of issues, that is, decomposition of the perovskite material, perovskite/electrode interface degradation, degradation of the morphology, etc. The perovskite material and electrode/perovskite interfacial degradation can be readily observed (Figure S6, Supporting Information) because only parts of the perovskite film are covered by the electrodes. The decomposition of the perovskite structure is usually clearly evident in the color, that is, the perovskite turns from dark brown to yellow. As seen in the photo image (Figure S6, Supporting Information), the color of all the present Cl^- incorporated perovskite films remains dark after the 85 °C/65 RH% damp heat treatment. In contrast, the color of Ag electrode turns visibly dark in the Cl^--free perovskite devices. We hence surmise that the degradation of the perovskite/electrode interface dominates the efficiency drop. In this case the electrode may accelerate the decomposition or degrade the morphology of the underlying perovskite layer, or both mechanisms may be playing an active role. We also performed light soaking tests for both the $MAPbI_3$ and Cl^- incorporated devices. However, the devices with differing perovskite film compositions show similar degradations, indicating that Cl^- incorporation has no significant effect on the suppression of light-induced degradation. For a 12% module encapsulated with epoxy-sealed glass, a superior stability of >90% PCE is recorded under ambient conditions (≈70 RH% and room temperature) over 1500 h as shown in Figure S7 (Supporting Information).

Spin-coating techniques offer the attraction of good thin film uniformity for lab-scale cell demonstrations. However, they have limitations in large throughput production and materials transfer efficiency, that is, high percentages of solution are wasted during coating. For large-area, high-speed manufacturing, coating techniques such as slot-die coating, spray-coating, dip-coating, doctor-blade coating, etc., are usually employed. Here, we show the adaptability of the present hot-casting system to these industrial large-scale coating techniques by demonstrating a "hot dip-coating" process. From the images shown in Figure 4d, it can be seen that the perovskite crystallizes on the substrate instantly as the substrate is withdrawn from the solution. The entire process is shown as a video in the Supporting Information. The perovskite thin film yields the photovoltaic performance of J_{sc} = 20.68 mA cm^{-2}, V_{oc} = 1.00 V, FF = 60.2%, and PCE = 12.4%. Note that dip-coating is one of the mature large-scale coating technologies in industry and compatible with ultrafast roll-to-roll production. However, dip-coating usually yields thicker films (≈tens or hundreds of μms) with rougher surfaces than other coating techniques, presenting specific challenges for perovskites, owing to the strict requirements for film thickness (≈300 nm) and uniformity. In the present work, the dip-coated film thickness is ≈1 μm by profilometry, which is ≈3× thicker than the spin-coated films. From the PCE of ≈12% achieved here by dip-coating, we expect even higher device performance from commercial techniques such as slot-die coating with better control film thickness and roughness. This suggests that perovskite hot-casting can be directly implemented in high throughput production lines using slot-die or spray-coating to commercialize perovskite technology.

3. Conclusions

Control of Cl^- incorporation significantly enhances hot-cast perovskite film optoelectronic properties, thin film quality, and environmental stability. Excellent PCE performance of 18.2% for small 0.09 cm^2 area and 15.4% for large ≈1 cm^2 area cells is achieved. High-efficiency large-area modules with PCE ≈12.0% were also demonstrated. The hot dip-coating variant demonstrates the viability of a hot-casting system in large-throughput coating techniques for potential commercialization.

4. Experimental Section

Spin-Coated Solar Cell Device Fabrication: FTO-coated glass substrates (Hartford, TEC7) were cleaned by sequential sonication in detergent, methanol, and isopropanol, followed by a 15 min UV–ozone treatment. The hole transporter NiO_x was deposited according to methodology reported elsewhere.[48] $MAPbI_3$ perovskite solutions were prepared by dissolving lead iodide (FrontMaterials Co. Ltd.) and methylammonium iodide (FrontMaterials Co. Ltd.) and perovskite solutions with Cl^- incorporation were additionally charged with 3, 5, 10, and 20 at% $PbCl_2$ (Aldrich, 99.999%) and MACl (Alfa Aesar, 99%) with respect to $MAI + PbI_2$. The details of the solution preparation can be found in Table S1 (Supporting Information). All the solutions were then stirred for 1 h at 70 °C prior to use. The FTO/NiO_x substrates were next preheated at 180 °C on a hot plate and transferred to a coater. Around 100 µL perovskite solution was quickly dropped onto the hot substrate followed by spin-coating at 4000 rpm for 15 s. The solution turned black in ≈4–5 s, indicating perovskite crystallization. Monitoring of the substrate temperature was performed sequentially, that is, 2, 5, 10, and 15 s with a thermocouple as shown in Figure S8 (Supporting Information). A $PC_{61}BM$ (FrontMaterials Co. Ltd. 99.5%) solution of 20 $mgmL^{-1}$ in chlorobenzene was then spin-coated on the perovskite at 1000 rpm for 30 s. The work function modifier polyethylenimine (PEI) in isopropanol was subsequently spin-coated onto the $PC_{61}BM$. Devices were completed by thermal evaporation of 100 nm silver electrodes with active areas of 0.09 cm^2. The large-area cell ≈1 cm^2 was fabricated on a layout of 1 cm × 1 cm as shown in the inset of Figure 4a. All the spin-coating processes were performed in a humidity controlled box with purged with dry air at RH ≈3%.

Spin-Coated Solar Module Device Fabrication: The design of eight-cell connected modules is shown in Figure S5 (Supporting Information) for both top and side views of P1–P3 processes. Note the figure is a representative illustration with only five cells connected and not the same as the dimensions of real module. For the P1 process (Figure S5a, Supporting Information), the substrate was etched by 2 M hydrochloric acid and Zn powder with ITO stripes being masked by polyimide tape. The NiO_x/perovskite/$PC_{61}BM$/PEI layers were spin-coated on the substrate. For the P2 process, the isolation was performed manually by using knife blade (Figure S5b, Supporting Information). A 100 nm Ag layer was then thermally evaporated followed by the P3 process of manual scribing by the knife blade again (Figure S5c, Supporting Information).

Dip-Coated Solar Cell Device Fabrication: The concentration of perovskite solution was diluted to 0.4 M, with other experimental conditions the same as for spin-coating. The preheated substrate was removed from the hot plate, dipped into the solution and quickly pulled out. The perovskite crystallized on the heat substrate within 5 s as indicated by the color change from yellow to dark black. The whole process was recorded in a video shown in the Supporting Information.

Characterization of Perovskite Solar Cell/Module Devices: Solar cells were tested in air with shadow mask of 0.09 cm^2 for small-area cell and 1 cm^2 for large-area cell under A.M. 1.5 radiation (100 mW cm^{-2}) using an ABET solar simulator source and a Keithley 2400 source meter. The light source of solar simulator is a xenon arc lamp of a Spectra-Nova Class A instrument, with the intensity calibrated by using an NREL-certified monocrystalline Si diode coupled to a KG3 filter to get a spectral mismatch to unity. The *J–V* curves were obtained from voltage scans in both forward and backward directions with integration time of 1NPLC: 1NPLC for 60 Hz of 16.67 ms. The settling time was 0. The backward and forward scans are set within 1.2 and 0.0 V with 100 points. Measurements were performed in air and at room temperature. The EQE spectrum was acquired by an Oriel model QE-PV-SI instrument equipped with a NIST-certified Si diode.

Cross-sectional TEM samples were processed from an actual solar cell device using an FEI Helios Nanolab Dual Beam scanning electron and focused ion beam microscope. Briefly, a 200 nm electron beam deposits a Pt layer, followed by a 1.5 µm ion beam deposited Pt layer, used to protect the sample from ion damage. The samples were then cut, lifted out, mounted on a Cu TEM grid, and finally thinned to a thickness less than 100 nm. TEM imaging was performed with a JEOL-2100F transmission electron microscope. A Gatan CCD camera was employed to take the bright field images. A high-angle annular dark-field scanning TEM (STEM) detector combined with an Oxford EDS system were utilized to take the dark-field image and the EDS spectra, respectively.

For stability testing of the solar cells, the as-fabricated devices were placed on an 85 °C hot plate in a humidity controlled box with a relative humidity of 65%. The devices were kept in the dark and under open circuit conditions. The inert atmosphere stability tests for the module were conducted by storing the encapsulated module (UV-curable epoxy and glass) under ambient conditions (≈25 °C, ≈70% relative humidity) also in the dark and under open circuit conditions.

For the CE measurements, the white light was provided by a ring of white LEDs (Lumileds, 1 W) connected in series with a DC power supply (BK Precision). The LEDs were controlled by a fast switching MOSFET (Vishay, Si7116DN). The time resolution of the charge extraction measurement is limited by the turn-off time of the LEDs, which was less than 200 ns, tested by a silicon photodetector (Thorlabs, DET100A). During each measurement the LEDs were on for 200 ms to ensure charge saturation of the solar cells, and then turned off, with intensity controlled by a neutral density filter wheel (NDC-100C, Thorlabs). The transient voltage across a 50 Ω resistor connected in series with the solar cell was subsequently monitored and recorded using an oscilloscope (Tektronix TDS2014C). The total charge stored in the solar cell was obtained by integration of the decaying current. For the TPV measurements, the white light bias was provided by a Xenon arc lamp (Oriel), with intensity controlled by a neutral density filter wheel (NDC-100C, Thorlabs). The light perturbation was provided by the same LED rings used in the charge extraction measurements. The duration of the light perturbation was controlled to be ≈500 ns. The intensity of the light perturbation was varied to maintain a maximal transient photovoltage of ≈10–15 mV. The photovoltage decay was monitored and recorded by an oscilloscope with an input impedance of 1M Ω. In both measurements the light intensity was calibrated by a Rodboud University of Nijmegen certified monocrystalline Si cell (RK5N4324).

Characterization of Perovskite Films: Morphological characterizations were performed by OM (Nikon, L-UEPI), SEM (Hitachi SU8030, voltage: 20 kV, working distance: 5.2 mm), and AFM (Bruker Dimensional Icon). The crystal structures of the perovskite films were characterized by a Rigaku MiniFlex 600 X-ray diffractometer (Cu Kα, 1.5406 Å) operating at 40 kV and 15 mA. The TRPL data were collected at room temperature using a streak camera system (Hamamatsu C4334 Streakscope). The instrument response function (IRF) is ≈30 ps. After deconvolution fitting, the temporal resolution is ≈10 ps. An ultrafast amplifier (Spirit, Spectra-Physics) produces the fundamental beam of 1040 nm (100 kHz, 300 fs). It is used to pump a non-collinear optical parametric amplifier (Spirit-NOPA-3H, Spectra-Physics) which delivers tunable high repetition rate pulses with pulse widths as short as sub-20 fs; 575 nm laser pulses generated by the NOPA were used as the excitation source for all samples. Fluorescence quenching measurements were performed to estimate the electron and hole diffusion lengths by depositing additional quencher layers for electrons ($PC_{61}BM$) and holes (PEDOT:PSS) on

top and bottom of the perovskite films, respectively. The fluorescence decays of the pristine perovskite films are fit using a second-order recombination model described by Equation (1). The fluorescence decays of the perovskite/PC_{61}BMTCNQ and perovskite/PEDOT:PSS films are then fit according to a 1D diffusion model, Equation (2)

$$\frac{dN}{dt} = -k_1 N - k_2 N^2 \quad (1)$$

$$\frac{\partial n(x,t)}{\partial t} = D\frac{\partial^2 n(x,t)}{\partial x^2} - k_{eff} n(x,t) \quad (2)$$

$$k_{eff} = -\frac{1}{N}\frac{dN}{dt} = k_1 + k_2 N \quad (3)$$

where k_1 is the first-order rate constant for single carrier trapping (trap state-mediated recombination) and k_2 is the second-order rate constant for free carrier (electrons and holes) recombination.[49] D is the diffusion coefficient and k_{eff} is the "effective first-order" recombination rate constant in the pristine $CH_3NH_3PbI_3$ films, defined according to Equation (3).[50] The electron and hole diffusion lengths were then calculated by $L_D = \sqrt{D\tau} = \sqrt{D/k_{eff}}$ .z.

Supporting Information

Supporting Information is available from the Wiley Online Library or from the author.

Acknowledgements

This research was supported in part by Argonne-Northwestern Solar Energy Research (ANSER) Center, an Energy Frontier Research Center funded by the U.S. Department of Energy, Office of Science, Office of Basic Energy Sciences under Award No. DE-SC0001059 (perovsktie opto-electronic and microstructural characterizations) and by the U.S. Department of Energy, Office of Science, and Office of Basic Energy Sciences under Award No. DE-FG02-08ER46536, and by the Institute for Sustainability and Energy at Northwestern (ISEN) (spectroscopic instrumentation). The financial support from Ministry of Science and Technology (105-3113-E-002-010) (perovskite solar cell fabrication) is highly appreciated.

Received: July 28, 2016
Revised: November 12, 2016
Published online: December 20, 2016

[1] M. A. Green, A. Ho-Baillie, H. J. Snaith, *Nat. Photonics* **2014**, *8*, 506.
[2] P. Gao, M. Gratzel, M. K. Nazeeruddin, *Energy Environ. Sci.* **2014**, *7*, 2448.
[3] M. A. Green, K. Emery, Y. Hishikawa, W. Warta, E. D. Dunlop, *Prog. Photovoltaics* **2015**, *23*, 1.
[4] S. Kazim, M. K. Nazeeruddin, M. Gratzel, S. Ahmad, *Angew. Chem., Int. Ed.* **2014**, *53*, 2812.
[5] W. Chen, Y. Z. Wu, Y. F. Yue, J. Liu, W. J. Zhang, X. D. Yang, H. Chen, E. B. Bi, I. Ashraful, M. Gratzel, L. Y. Han, *Science* **2015**, *350*, 944.
[6] M. A. Green, K. Emery, Y. Hishikawa, W. Warta, E. D. Dunlop, *Prog. Photovoltaics* **2015**, *23*, 805.
[7] X. Li, D. Q. Bi, C. Y. Yi, J. D. Decoppet, J. S. Luo, S. M. Zakeeruddin, A. Hagfeldt, M. Gratzel, *Science* **2016**, *353*, 58.
[8] Q. Wang, Q. Dong, T. Li, A. Gruverman, J. Huang, *Adv. Mater.* **2016**, *28*, 6734.
[9] J. T.-W. Wang, Z. Wang, S. Pathak, W. Zhang, D. W. deQuilettes, F. Wisnivesky-Rocca-Rivarola, J. Huang, P. K. Nayak, J. B. Patel, H. A. Mohd Yusof, Y. Vaynzof, R. Zhu, I. Ramirez, J. Zhang, C. Ducati, C. Grovenor, M. B. Johnston, D. S. Ginger, R. J. Nicholas, H. J. Snaith, *Energy Environ. Sci.* **2016**, *9*, 2892.
[10] N. J. Jeon, J. H. Noh, Y. C. Kim, W. S. Yang, S. Ryu, S. I. Seol, *Nat. Mater.* **2014**, *13*, 897.
[11] H. H. Tsai, W. Y. Nie, P. Cheruku, N. H. Mack, P. Xu, G. Gupta, A. D. Mohite, H. L. Wang, *Chem. Mater.* **2015**, *27*, 5570.
[12] W. Y. Nie, H. H. Tsai, R. Asadpour, J. C. Blancon, A. J. Neukirch, G. Gupta, J. J. Crochet, M. Chhowalla, S. Tretiak, M. A. Alam, H. L. Wang, A. D. Mohite, *Science* **2015**, *347*, 522.
[13] A. T. Barrows, A. J. Pearson, C. K. Kwak, A. D. F. Dunbar, A. R. Buckley, D. G. Lidzey, *Energy Environ. Sci.* **2014**, *7*, 2944.
[14] Y. Deng, E. Peng, Y. Shao, Z. Xiao, Q. Dong, J. Huang, *Energy Environ. Sci.* **2015**, *8*, 1544.
[15] Y. C. Liu, Z. Yang, D. Cui, X. D. Ren, J. K. Sun, X. J. Liu, J. R. Zhang, Q. B. Wei, H. B. Fan, F. Y. Yu, X. Zhang, C. M. Zhao, S. Z. Liu, *Adv. Mater.* **2015**, *27*, 5176.
[16] Y. Zhao, K. Zhu, *J. Phys. Chem. C* **2014**, *118*, 9412.
[17] S. Colella, E. Mosconi, P. Fedeli, A. Listorti, F. Gazza, F. Orlandi, P. Ferro, T. Besagni, A. Rizzo, G. Calestani, G. Gigli, F. De Angelis, R. Mosca, *Chem. Mater.* **2013**, *25*, 4613.
[18] K. W. Tan, D. T. Moore, M. Saliba, H. Sai, L. A. Estroff, T. Hanrath, H. J. Snaith, U. Wiesner, *ACS Nano* **2014**, *8*, 4730.
[19] B. W. Park, B. Philippe, T. Gustafsson, K. Sveinbjornsson, A. Hagfeldt, E. M. J. Johansson, G. Boschloo, *Chem. Mater.* **2014**, *26*, 4466.
[20] Q. Dong, Y. Yuan, Y. Shao, Y. Fang, Q. Wang, J. Huang, *Energy Environ. Sci.* **2015**, *8*, 2464.
[21] M. I. Dar, N. Arora, P. Gao, S. Ahmad, M. Gratzel, M. K. Nazeeruddin, *Nano Lett.* **2014**, *14*, 6991.
[22] H. Yu, F. Wang, F. Y. Xie, W. W. Li, J. Chen, N. Zhao, *Adv. Funct. Mater.* **2014**, *24*, 7102.
[23] S. T. Williams, F. Zuo, C. C. Chueh, C. Y. Liao, P. W. Liang, A. K. Y. Jen, *ACS Nano* **2014**, *8*, 10640.
[24] S. D. Stranks, G. E. Eperon, G. Grancini, C. Menelaou, M. J. P. Alcocer, T. Leijtens, L. M. Herz, A. Petrozza, H. J. Snaith, *Science* **2013**, *342*, 341.
[25] G. C. Xing, N. Mathews, S. Y. Sun, S. S. Lim, Y. M. Lam, M. Gratzel, S. Mhaisalkar, T. C. Sum, *Science* **2013**, *342*, 344.
[26] E. Edri, S. Kirmayer, A. Henning, S. Mukhopadhyay, K. Gartsman, Y. Rosenwaks, G. Hodes, D. Cahen, *Nano Lett.* **2014**, *14*, 1000.
[27] C. Wehrenfennig, G. E. Eperon, M. B. Johnston, H. J. Snaith, L. M. Herz, *Adv. Mater.* **2014**, *26*, 1584.
[28] Y. Tidhar, E. Edri, H. Weissman, D. Zohar, G. Hodes, D. Cahen, B. Rybtchinski, S. Kirmayer, *J. Am. Chem. Soc.* **2014**, *136*, 13249.
[29] E. L. Unger, A. R. Bowring, C. J. Tassone, V. L. Pool, A. Gold-Parker, R. Cheacharoen, K. H. Stone, E. T. Hoke, M. F. Toney, M. D. McGehee, *Chem. Mater.* **2014**, *26*, 7158.
[30] P. Docampo, F. C. Hanusch, S. D. Stranks, M. Doblinger, J. M. Feckl, M. Ehrensperger, N. K. Minar, M. B. Johnston, H. J. Snaith, T. Bein, *Adv. Energy Mater.* **2014**, *4*, 1400355.
[31] F. X. Xie, D. Zhang, H. M. Su, X. G. Ren, K. S. Wong, M. Gratzel, W. C. H. Choy, *ACS Nano* **2015**, *9*, 639.
[32] S. Colella, E. Mosconi, G. Pellegrino, A. Aberti, V. L. P. Guerra, S. Masi, A. Listorti, A. Rizzo, G. G. Condorelli, F. De Angelis, G. Gigli, *J. Phys. Chem. Lett.* **2014**, *5*, 3532.
[33] D. E. Starr, G. Sadoughi, E. Handick, R. G. Wilks, J. H. Alsmeier, L. Kohler, M. Gorgoi, H. J. Snaith, M. Bar, *Energy Environ. Sci.* **2015**, *8*, 1609.
[34] G. Pellegrino, S. Colella, I. Deretzis, G. G. Condorelli, E. Smecca, G. Gigli, A. La Magna, A. Alberti, *J. Phys. Chem. C* **2015**, *119*, 19808.

[35] C. C. Stoumpos, C. D. Malliakas, M. G. Kanatzidis, *Inorg. Chem.* **2013**, *52*, 9019.
[36] J. Qing, H. T. Chandran, Y. H. Cheng, X. K. Liu, H. W. Li, S. W. Tsang, M. F. Lo, C. S. Lee, *ACS Appl. Mater. Interfaces* **2015**, *7*, 23110.
[37] M. Liu, M. B. Johnston, H. J. Snaith, *Nature* **2013**, *501*, 395.
[38] E. Mosconi, A. Amat, M. K. Nazeeruddin, M. Gratzel, F. De Angelis, *J. Phys. Chem. C* **2013**, *117*, 13902.
[39] Q. Chen, H. P. Zhou, T. B. Song, S. Luo, Z. R. Hong, H. S. Duan, L. T. Dou, Y. S. Liu, Y. Yang, *Nano Lett.* **2014**, *14*, 4158.
[40] D. Y. H. Cao, C. C. Stoumpos, C. D. Malliakas, M. J. Katz, O. K. Farha, J. T. Hupp, M. G. Kanatzidis, *Appl. Mater.* **2014**, *2*, 091101.
[41] M. T. Trinh, X. X. Wu, D. Niesner, X. Y. Zhu, *J. Mater. Chem. A* **2015**, *3*, 9285.
[42] D. Shi, V. Adinolfi, R. Comin, M. J. Yuan, E. Alarousu, A. Buin, Y. Chen, S. Hoogland, A. Rothenberger, K. Katsiev, Y. Losovyj, X. Zhang, P. A. Dowben, O. F. Mohammed, E. H. Sargent, O. M. Bakr, *Science* **2015**, *347*, 519.
[43] M. D. Irwin, J. D. Servaites, D. B. Buchholz, B. J. Leever, J. Liu, J. D. Emery, M. Zhang, J. H. Song, M. F. Durstock, A. J. Freeman, M. J. Bedzyk, M. C. Hersam, R. P. H. Chang, M. A. Ratner, T. J. Marks, *Chem. Mater.* **2011**, *23*, 2218.
[44] J. Chae, Q. Dong, J. Huang, A. Centrone, *Nano Lett.* **2015**, *15*, 8114.
[45] Y. Shao, Z. Xiao, C. Bi, Y. Yuan, J. Huang, *Nat. Commun.* **2014**, *5*, 5784.
[46] J. D. Servaites, S. Yeganeh, T. J. Marks, M. A. Ratner, *Adv. Funct. Mater.* **2010**, *20*, 97.
[47] Y. Kato, L. K. Ono, M. V. Lee, S. H. Wang, S. R. Raga, Y. B. Qi, *Adv. Mater. Interfaces* **2015**, *2*, 1500195.
[48] J. Y. Jeng, K. C. Chen, T. Y. Chiang, P. Y. Lin, T. D. Tsai, Y. C. Chang, T. F. Guo, P. Chen, T. C. Wen, Y. J. Hsu, *Adv. Mater.* **2014**, *26*, 4107.
[49] M. T. Trinh, X. Wu, D. Niesner, X. Y. Zhu, *J. Mater. Chem. A* **2015**, *3*, 9285.
[50] O. V. C. La, T. Salim, J. Kadro, M. T. Khuc, R. Haselsberger, L. Cheng, H. Xia, G. G. Gurzadyan, H. Su, Y. M. Lam, R. A. Marcus, M. E. Michel-Beyerle, E. E. Chia, *Nat. Photonics* **2015**, *6*, 7903.